Evolution of Microstructure and Residual Stress for a Lead-Frame Cu-2.13fe-0.026 P (Wt%) Alloy

Taifeng Cao[1], Shaohua Wang[2], G. Zhao, X. L. Wu, Peter K. Liaw[3], and Junwei Qiao[1, 4, *]

[1]*College of Materials Science and Engineering, Taiyuan University of Technology, Taiyuan 030024, China*

[2]*TAIYUAN JINXI CHUNLEI COPPER Company Limited, Taiyuan 030024, China*

[3]*Department of Materials Science and Engineering, The University of Tennessee, Knoxville, TN, 37996-2200, USA*

[4]*Key Laboratory of Interface Science and Engineering in Advanced Materials, Ministry of Education, Taiyuan University of Technology, Taiyuan 030024, China*

[*]*Corresponding author. E-mail address: qiaojunwei@gmail.com (J.W. Qiao)*

ABSTRACT

The lead frame C19400 strips are warped during the etching process due to the presence of the residual stress. Therefore, it is essential to eliminate the residual stress of the C19400 strips. The microstructure, residual stress, and mechanical properties of the C19400 alloy were studied after different stress relieving annealing. After annealing at 300 °C for 5 minutes, the microhardness of the alloy increased to 148.6 HV, and the residual stress decreased from 125.9 MPa (RD) and 137.1 MPa (TD) to 13.2 MPa (RD) and 16.5 MPa (TD), with a decrease rate of 89.5% (RD) and 87.9% (TD). Residual stress is mainly released through thermal activation during the low-temperature recovery process. Furthermore, as the temperature increases, the α-Fe precipitates grow from 31 nm at 300 °C to 82 nm at 500 °C. Following annealing at 500 °C, the alloy undergoes recrystallization, resulting in a rapid decrease in mechanical properties and still high residual stress. This trend is considered to be due to the uneven distributions of the grain size and orientation caused by high temperature, further leading to plastic mismatch.

Keywords

C19400 lead frame; Residual stress; Stress relieving annealing; α-Fe

Introduction

Semiconductor integrated circuits [1, 2] are the core devices of electronic products, and the development of their industrial technology directly affects the level of the power industry. As an important component of integrated circuits, the lead frame [3] serves to connect the circuit with the chip. It not only transmits the information of chip, but more importantly, dissipates the heat generated by the circuit. The lead frame material needs to meet certain conditions [4-7], such as high strength, high conductivity and thermal conductivity. Among many materials, copper alloys [8-10] are known for their superior thermal and electrical conductivity. And through appropriate plastic deformation processes such as rolling [11, 12], equal channel angular pressing [13, 14] and high pressure torsion [15, 16], the tensile strength of copper alloys can be greatly improved. Therefore, at present, the lead frame material is mainly copper alloy, especially Cu-Fe-P alloy [17, 18]. Because the Cu-Fe-P alloy not only possesses the excellent properties mentioned above, but also has a lower cost. As the most representative Cu-Fe-P alloy, C19400 alloy was developed earliest and is currently the most commonly utilized [19].

When preparing lead frame materials, the C19400 alloy usually undergoes multiple processes including rolling, aging annealing and etching [4]. During the plastic deformation process of the strip, uneven plastic deformation occurs inside the strip due to factors, such as friction between rollers and strips, roller pressure, and roller speed, resulting in residual stress inside the strip [20, 21]. The presence of residual stress can cause surface warping behavior of the C19400 alloy during the etching process of the finished product. Eventually, the C19400 alloy strip will fail and become unusable. Therefore, it is urgent to find a suitable method to eliminate residual stress inside the strip material.

The methods for eliminating and adjusting residual stresses are mainly divided into mechanical action and heat treatment. Mechanical-action methods reduce residual stresses by causing yield effects in the residual-stress area of the material. Mechanical methods mainly include hammering [22, 23], vibration aging [24, 25], and stretch-bending straightening [26]. After being processed by these methods, the residual stress can be effectively reduced. For example, the residual stress of the C19400 alloy can be reduced by about 86% through selecting appropriate tension and straightening parameters [27]. However, due to the need for more precise equipment, the cost of using mechanical methods to eliminate residual stresses is relatively high. Secondly, the mechanical method inevitably reduces the dimensional accuracy of copper strips and reduces the surface flatness of copper strips during the process of eliminating residual stresses. Therefore, mechanical techniques have not been widely used in eliminating residual stresses of copper strips. Then, in addition to mechanical methods, heat treatment is often utilized to eliminate residual stresses of various materials. For instance, it was found that the residual stress of the TC4 alloy produced by laser additive manufacturing decreased after the heat treatment. And the temperature and cooling rate are the main factors affecting the residual stress [28]. Furthermore, relevant literature has reported the effect of heat treatment on residual stresses of Al-6061 rods [29]. These results indicate that heat treatment reduces residual stresses of Al-6061 rods and creates a symmetrical balance between compressive and tensile stresses. In the study of the effect of heat treatment on residual stresses in SiCp/Al-Cu-Mg materials [30], it was found that the effect of heat treatment temperature on residual stresses is much more important than other factors. The increasement of the heat-treatment temperature will make residual stresses decrease. Thus, it can be seen that using heat-treatment methods to reduce materials' residual stresses is feasible. However, it is worth noting that there are few reports studying the effect of heat treatment on residual stresses in the C19400 alloy. The effect of stress-relieving annealing on the C19400 alloy is not quite clear. The mechanism of the residual-stress release is also unknown. Therefore, it is necessary to conduct research on stress-relieving annealing of the C19400 alloy.

In this study, a high-precision nanoindentation technology was used to evaluate the residual stress of the C19400 alloy. The dislocation distribution, precipitates' size and volume fraction inside the alloy after stress-relieving annealing were further characterized. More importantly, this study provides a more suitable stress-relieving annealing process by studying the evolution of the microstructure, residual stress, and microhardness of the alloy. Finally, the residual stress-release mechanism was discussed in detail from the perspective of dislocations and precipitates.

Experimental procedures

The initial state of the commercial C19400 alloy is hot rolled, provided by *the Taiyuan Jinxi Chunlei Copper Company Limited.* The specific chemical composition of the C19400 alloy contained 2.13 weight percent (wt.%) iron, 0.026 wt.% phosphorus and balance copper. Copper alloys with the same chemical composition can be found in our previous work [31]. Firstly, the hot-rolled plate with a thickness of 8 mm is cold rolled at room temperature to a thickness of 0.8 mm (90% deformation rate), with each reduction of 0.3 mm. To ensure the uniformity of the rolling process, after each pass of rolling is completed, the alloy plate is flipped 180 ° before proceeding to the next pass of rolling. Then, the 0.8 mm thickness strip was annealed at 200 ℃, 300 ℃, 400 ℃, and 500 ℃ for 5 minutes, 60 minutes, 300 minutes and 480 minutes, respectively, and subsequently cooled in air to room temperature.

The residual stress of the copper strip was tested by the Hysitron TI Premier Nanoindenter (Bruker, Minneapolis, MN, USA) with a Berkovich diamond pyramid tip at room temperature. The maximum load is 10 mN, the load holding time is 2 s, and the loading rate is 2 mN/s. These indentation experiments with an array of 2 × 3 grid indents were carried out on each specimen and the interval between two points was 20 µm. For standardization, residual-stress values are presented in absolute values. Phase characterization and dislocation density were analyzed by X-ray diffraction (XRD) using a PANalytical diffractometer with Cu-Ka radiation. The microstructures were performed by Phenom XL scanning electron microscopy (SEM). The precipitates' distribution and dislocation configuration were characterized by JEOL F200 transmission electron microscope (TEM) with a maximum acceleration voltage of 200 kV. TEM thin foils were prepared by twin jet polishing (Tenupol-5, Struers) in a 75% methanol + 25% nitric acid solution at 10 V and - 30 °C. The precipitates' sizes were counted by the Image-Pro Plus 6.0 software. Microhardness measurements were conducted on an MH-600 digital microhardness tester with a load of 200 g for 15 s. For each sample, 5 points were measured , and the results were averaged.

Results

Mechanical properties

Figure 1 exhibits the microhardness curves of the C19400 alloy with a deformation of 90% and after annealing under different processes. The specific microhardness values are displayed in Table 1. From Figure 1 and Table 1, it can be seen that the alloy has a microhardness of 143.4 HV after undergoing 90% cold-rolling deformation. Then, the alloy deformed to 90% is annealed at 200 °C. It can be observed that as the annealing time increases, the microhardness of the alloy will gradually decrease. After annealing at 200 °C for 480 minutes, the microhardness of the alloy decreased from 143.4 HV to 139.4 HV. Subsequently, the alloy with a deformation of 90% was annealed at 300 °C. It can be observed that when the alloy is annealed at 300 °C, the microhardness of the alloy does not show a gradual decrease trend with the extension of the annealing time. After annealing at 300 °C for 5 minutes, the microhardness of the alloy increased from 143.4 HV to 148.6 HV. Then, as time increases, the microhardness gradually decreases. After annealing at 300 ℃ for 480 minutes, the microhardness of the alloy decreased to 137.8 HV. When annealing the 90%-deformed alloy at 400 ℃, the trend of the microhardness change of the alloy is consistent with that at 300 ℃. As the annealing time increases, the microhardness of the alloy first increases at 5 minutes, and then gradually decreases with the extension of time. Unlike annealing at 300 ℃, the microhardness of the alloy annealed at 400 ℃ for 480 minutes is 129.9 HV, which decreases more than that of annealing at 300 ℃ for 480 minutes. This result shows that the higher the annealing temperature, the more significant the decrease in microhardness. Similar results have been found in other reports [32-34]. It is worth noting that a significant change occurs when the alloy with a deformation rate of 90% is annealed at 500 ℃. When annealed at 500 ℃ for 5 minutes, the microhardness of the alloy decreased from 143.4 HV to 140.6 HV. However, when prolonged at 500 ℃, the microhardness of the alloy will significantly decrease. After annealing at 500 ℃ for 60 minutes, the microhardness of the alloy decreased from 143.4 HV to 97.6 HV, with a decrease rate of up to 32.2%. Then, as time continued to increase, the microhardness of the alloy gradually decreased and remained at 95.1 HV after annealing for 480 minutes. The decrease rates of microhardness of the alloy with a deformation rate of 90% after annealing at 200 ℃, 300 ℃, 400 ℃, and 500 ℃ for 480 minutes are 2.8%, 3.9%, 9.4% and 33.7%, respectively. It can be concluded that annealing at 200 ℃ and 300 ℃ has little effect on the microhardness of the alloy, while annealing at 500 ℃ can significantly reduce the microhardness of the alloy.

Residual stress after annealing

The elastic work model [35] using the nanoindentation technology is utilized to calculate the residual stress of the C19400 alloy after different annealing processes. The elastic-work model can be expressed by the following equation:

when the indenter of nanoindentation performs work:

$$W_{\mathrm{e}} = \int_{h_{\mathrm{f}}}^{h_{\max}} P(h)\,\mathrm{dh} = \int_{h_{\mathrm{f}}}^{h_{\max}} a(h\text{-}h_{\mathrm{f}})^{m}\,\mathrm{dh} = \frac{a(h_{\max}\text{-}h_{\mathrm{f}})^{\mathrm{m+1}}}{\mathrm{m+1}} = \frac{P_{\max}}{\mathrm{m+1}}(h_{\max}\text{-}h_{\mathrm{f}}) \quad (1)$$

when there is the compressive stress in alloys,

$$W_{\mathrm{e}}^{\mathrm{c}} - W_{\mathrm{e}}^{0} = (P_{\max}^{0} + \sigma_{\mathrm{res}} A_{\mathrm{c}} \sin\alpha \text{-} \mathrm{P}_{\max}^{0})(h_{\max}\text{-}h_{\mathrm{f}}) \quad (2)$$

when there is a tensile stress in alloys,

$$W_{\mathrm{e}}^{\mathrm{t}} - W_{\mathrm{e}}^{0} = (P_{\max}^{0} - \sigma_{\mathrm{res}} A_{\mathrm{c}} \text{-} \mathrm{P}_{\max}^{0})(h_{\max}\text{-}h_{\mathrm{f}}) \quad (3)$$

substituting Equation (1) into Equations (2) and (3):

the compressive stress:

$$\left(\frac{P_{\max}^{0}(h_{\max}\text{-}h_{\mathrm{f}})}{(m_0+1)} - \frac{P_{\max}^{c}(h_{\max}\text{-}h_{\mathrm{f}})}{(m_1+1)}\right) = (\sigma_{\mathrm{res}} A_{\mathrm{c}} \sin\alpha)(h_{\max}\text{-}h_{\mathrm{f}}) \quad (4)$$

the tensile stress:

$$\left(\frac{P_{\max}^{0}(h_{\max}\text{-}h_{\mathrm{f}})}{(m_0+1)} - \frac{P_{\max}^{t}(h_{\max}\text{-}h_{\mathrm{f}})}{(m_1+1)}\right) = (\sigma_{\mathrm{res}} A_{\mathrm{c}})(h_{\max}\text{-}h_{\mathrm{f}}) \quad (5)$$

simplifying Equations (4) and (5) as follows:

the compressive stress:

$$\sigma_r = \frac{\frac{P_0}{m_0+1} - \frac{P}{m_{\mathrm{U}}+1}}{\sin\alpha A_{\mathrm{c}}} \quad (6)$$

The tensile stress:

$$\sigma_r = \frac{\frac{P_0}{m_0+1} - \frac{P}{m_{\mathrm{U}}+1}}{A_{\mathrm{c}}} \quad (7)$$

where W_e represents the work done by the indenter of the nanoindentation. $h_{\max}$ is the maximum contact depth obtained from nanoindentation testing. h_f is the final indentation depth on the alloy surface after the completion of the nanoindentation test. A_c is the contact area between the indenter and C19400 alloy. P is the load of nanoindentation. The fixed load, $P_{\max}$, used in this study is 10 mN. The superscripts "0", "c" and "t" are the stress free, compressive and tensile stresses, respectively. m is the power-law exponent of the unloading curve, and the subscripts "0" and "1" represent the stress free and stressed????, respectively. α is the angle of the indenter, which is a constant of 24.7°. σ_r is the residual stress of the C19400 alloy.

The residual-stress distribution of the C19400 alloy after annealing with different processes is shown in Figure 2. The residual stress was tested separately in the rolling direction (RD) and transverse direction (TD) of each sample. The specific residual-stress values are listed in Table 2. As displayed in Figure 2 and Table 2, all samples exhibit compressive stresses. The residual stresses of RD and TD after 90% rolling deformation of the sample are 125.9 MPa and 137.1 MPa, respectively. Then, the specimen with a deformation rate of 90% was annealed at 200 °C. As the annealing time increased, the residual stress gradually increased, reaching the maximum values of 253.5 MPa (RD) and 261.9 MPa (TD) at 300 minutes. Then, when the annealing time increases to 480 minutes, the residual stress decreases to 211.2 MPa (RD) and 229.9 MPa (TD), as displayed in Figure 2(a). It is worth noting that after annealing at 200 °C, the residual stress of the alloy did not decrease but instead increased.

Furthermore, there is a slight difference in the residual stress between the rolling direction (RD) and transverse direction (TD). Similar phenomena have been found in other reports [36, 37]. Next, the 90%-deformed alloy was annealed at 300 ℃ for different times, seen in Figure 2(b). It was found that when annealed at 300 ℃ for 5 minutes, there was a significant decrease in the residual stress in both the rolling direction and transverse direction of the alloy. After annealing for 5 minutes, the residual stress decreased from 125.9 MPa (RD) and 137.1 MPa (TD) to 13.2 MPa (RD) and 16.5 MPa (TD), with a decrease rate of 89.5% (RD) and 87.9% (TD), respectively. However, when the annealing time increased to 60 minutes, the residual stress increased to 191.3 MPa (RD) and 189.6 MPa (TD), even higher than the alloy with a rolling deformation rate of 90%. As the annealing time continues to increase, the residual stress of the alloy gradually decreases. And at 480 minutes, the residual stress of the alloy decreased to the minimum values of 9.9 MPa (RD) and 12.3 MPa (TD). Compared with annealing at 200 ℃, the residual stress after annealing at 300 ℃ is generally lower. Figure 2(c) depicts the residual-stress distribution of the alloy after annealing at 400 ℃ for different time. It can be seen that the trend of the residual-stress change after annealing at 400 ℃ is consistent with that at 200 ℃. As the annealing time prolongs, the residual stress of the alloy first increases and then decreases. The maximum residual stress after annealing at 400 ℃ occurs at an annealing time of 60 minutes, with maximum values of 235.8 MPa (RD) and 228.3 MPa (TD). Then, after annealing at 400 ℃ for 300 minutes, the residual stress decreased significantly. After annealing for

300 minutes, the residual stress decreased to 32.3 MPa (RD) and 20.8 MPa (TD). Compared with annealing for 60 minutes, the residual-stress reduction rates of annealing for 300 minutes are 86.3% and 90.8%, respectively. As the annealing time increases to 480 minutes, the residual stress values stabilize at 22.6 MPa (RD) and 25.1 MPa (TD). Compared with alloys with a deformation rate of 90%, the residual stress reduction rates reached 82.1% and 81.7% after annealing at 400 ℃ for 480 minutes. Finally, the residual stress after annealing at 500 ℃ is exhibited in Figure 2(d). After annealing at 500 ℃, the evolution of the residual stress is similar to that at 300 ℃. The residual stress shows a trend of first decreasing, then increasing and then gradually decreasing. After annealing at 500 ℃ for 60 minutes, the residual stress of the alloy reached its maximum values of 145.8 MPa (RD) and 168.2 MPa (TD). And the stress value is still higher than that of alloys with a deformation rate of 90%. Further observation revealed that after annealing at 500 ℃ for 5 minutes, the residual stress reached the lowest values of 72.5 MPa (RD) and 66.1 MPa (TD). Compared to the alloy with a deformation rate of 90%, the residual-stress reduction rates were 42.4% and 51.8%. However, it is worth noting that after annealing at 500 ℃, the residual-stress value is generally higher. This result does not seem to show the characteristic that the higher the temperature, the lower the residual stress. This trend will be discussed in detail below.

Microstructure of C19400 alloy

Figures S1(a) and (b) demonstrate SEM images of the hot-rolled and 90%-deformed samples, respectively. From Figure S1(a), it can be seen that the grains of the hot-rolled sample are characterized by being parallel to the rolling direction. Due to the high-temperature during the hot-rolling process, the alloy undergoes recrystallization. According to statistics, the grain size of the hot-rolled samples is approximately 24.7 um. However, after 90%-cold-rolling deformation, the grains of the alloy are almost crushed, and dense grain boundaries are observed distributed along the rolling direction, as indicated in Figure S1(b). Similar results have been reported in relevant literatures [38-40].

Subsequently, the effect of different annealing processes on the microstructure of the C19400 alloy was studied. Figure S2 reveals the SEM images of the alloy with a deformation rate of 90% annealed at 200 ℃. As shown in Figure S2(a), after annealing at 200 ℃ for 5 minutes, the interior of the alloy is mainly composed of block shaped recovery grains. The grain boundaries are still relatively dense and mainly propagate parallel to the rolling direction. It is worth noting that after annealing at 200 ℃ for 5 minutes, no recrystallized grains were observed. Further observation revealed the presence of some precipitates inside the alloy, mainly composed of Fe_3P particles. This trend has been confirmed in our previous work, and specific details can be found in our previous study [31]. Then, as the annealing time increased to 60 minutes, 300 minutes, and 480 minutes, there was no significant change in the microstructure of the alloy, as seen in Figures S2(b), (c), and (d). The difference is that as the annealing time increases, the block grains inside the alloy tend to become larger, but there is still no recrystallization phenomenon, even after annealing at 200 °C for 480 minutes.

Figure 3 indicates the SEM image of the 90%-deformed alloy after annealing at 300 °C. From Figures 3(a)-(d), it can be exhibited that the alloy did not undergo recrystallization after annealing at 300 °C for different times. The microstructure is mainly composed of restored grains. After annealing at 300 °C for 300 minutes, it can be observed that the blocky grains of the alloy seem to become more obvious, and the grain boundaries gradually appear. It is worth noting that most grains undergo a recovery process mainly along the rolling direction.

The SEM image annealed at 400 °C is exhibited in Figure S3. Unlike 200 °C and 300 °C, after annealing at 400 °C, the alloy has more blocky grains and gradually grows. Especially after annealing at 400 °C for 300 minutes, the grain boundaries of the alloy not only become obvious, but also the grains gradually appear, as seen in Figure S3(c). This feature indicates that the effect of temperature on the microstructure of the alloy is gradually manifested.

Then, the alloy was annealed at 500 °C, as displayed in Figure S4. After annealing at 500 °C for 5 minutes, the interior of the alloy is mainly composed of block-like restored grains. Then, some small spherical grains were observed, even though their proportion was very small. This small spherical grain was not observed at 200-400 °C. Interestingly, after annealing at 500 °C for 60 minutes, the grains of the alloy underwent significant changes. The recovered grains in the alloy gradually disappear, and the recrystallized grains become the main part. This feature indicates that 500 ℃ has reached the recrystallization temperature of the C19400 alloy. As the annealing time continues to increase, the recrystallized grains of the alloy gradually increase, and at 480 minutes, almost no recovered grains can be seen inside the alloy.

In summary, when annealing the C19400 alloy with 90%-rolling deformation at 200 - 400 ℃, the alloy mainly consists of restored grains, and no recrystallized grains appear. However, after annealing at 500 ℃ for 60 minutes, the alloy exhibited significant recrystallization grains, and the recrystallization phenomenon became more pronounced with the increase of the annealing time.

Discussion

Stress-relieving annealing [41-43] usually means reducing the residual stress of the alloy while ensuring that the mechanical properties of the alloy do not decrease. It can be clearly seen from Figure 2 that compared to 200 ℃, 400 ℃, and 500 ℃, the residual stress of the alloy after annealing at 300 ℃ is lower. Although the residual stress is relatively low after annealing at 400 ℃ for 300 minutes and 480 minutes, the hardness of the alloy decreases after annealing at 400 ℃ for 300 minutes and 480 minutes. From Figure 1, it can be seen that after annealing at 400 ℃ for 300 minutes and 480 minutes, the hardness of the alloy decreased to 136.7 HV and 129.9 HV. More importantly, the longer the annealing time, the greater the cost involved. Therefore, annealing at 400 ℃ for a long time can reduce the residual stress, but it will lead to a decrease in mechanical properties and an increase in cost.

However, compared to 400 °C, annealing at 300 °C for 5 minutes can effectively reduce the residual stress of the alloy. After annealing at 300 °C for 5 minutes, the residual-stress-reduction rate of the alloy is 89.5% (RD) and 87.9% (TD)，as shown in Figure 1 and Table 1. Furthermore, after annealing at 300 °C for 5 minutes, the hardness of the alloy did not decrease, but instead increased to 148.6 HV. This trend fully satisfies the conditions for stress-relieving annealing. More importantly, annealing for 5 minutes is a shorter time, and the cost will be greatly reduced. Then, after annealing at 300 °C for 480 minutes, the residual stress of the alloy also decreased. Compared to annealing at 400 °C for 480 minutes, the decrease in hardness is not significant. It is worth noting that the cost of 300 °C is also lower than 400 °C.

In summary, for the C19400 alloy, annealing at 300 °C for 5 minutes and 480 minutes is a more suitable stress-relieving annealing process. Therefore, it is necessary to conduct deep research on the precipitates and dislocation characteristics after annealing at 300 °C for 5 minutes and 480 minutes.

Precipitation behavior of the C19400 alloy during annealing

Figure 4 demonstrates the TEM image of the C19400 alloy annealed at 300 °C for 5 minutes. A large number of dislocations can be observed from Figures 4(a), (b), and (c). These dislocations tangle and accumulate with each other, forming dislocation cells. It is observed from Figure 4(a) that there are high dislocation density regions and low dislocation density regions inside the alloy. As is well known, the formation of dislocations usually means that the alloy undergoes plastic deformation. In this study, the alloy underwent 90% cold-rolling deformation, which is relatively large for copper alloys with a face-centered-cubic structure [44-46]. Therefore, after 90%-cold-rolling deformation, there will be a large number of dislocations inside the C19400 alloy. However, after annealing at 300 °C for 5 minutes, there were still a large number of dislocations inside the alloy, which may be due to the fact that there was no recrystallization phenomenon inside the alloy after annealing at 300 °C for 5 minutes, and the alloy mainly underwent a recovery process. This result corresponds to the SEM image displayed in Figure 3. Because if the alloy undergoes recrystallization, dislocations will decrease. Further observation reveals the presence of α-Fe precipitates within the alloy. In fact, the presence of dislocations is beneficial for the precipitation of the second phase during the annealing process. Because dislocations not only provide the nucleation energy, but also offer nucleation sites for the second phase. From Figures 4(c) and (d), it can be clearly observed that the Fe_3P precipitate with a size bigger than 500 nm. This characteristic is consistent with previous research results [31]. Then, high-resolution TEM (HRTEM) characterization was performed at the interface between the Fe_3P precipitate and the Cu matrix, as seen in Figure 4(e). The crystal-plane spacing of the Fe_3P precipitate and Cu matrix is 0.16 nm and 0.21 nm, respectively. The precipitated phase forms a phase interface with the matrix, as seen in Figure 4(e). The relationship between precipitates and the matrix can be determined by the mismatch degree of the interface [47-49]. The mismatch degree (δ) can be expressed as follows:

$$\delta = \frac{2(a_\alpha - a_\beta)}{(a_\alpha + a_\beta)}, \tag{8}$$

where a_α and a_β are the surface spacing between the two parallel interfaces of the second phase and the matrix, respectively. When $\delta < 0.05$, the two phases exhibit a coherent relationship; When $0.05 \leq \delta \leq 0.25$, the two phases exhibit a semi-coherent relationship; When $\delta > 0.25$, the two phases exhibit a non-coherent relationship. The mismatch degree between the Fe_3P precipitate and the matrix is calculated to be 0.27. Therefore, the relationship between the Fe_3P precipitate and the matrix is non-coherent.

It is worth noting that during the transmission-spot analysis of the alloy, the diffraction spot of the α-Fe precipitate was not observed, as shown in Figure 4(f). This trend may be caused by two reasons. Firstly, annealing at 300 ℃ for 5 minutes, due to the lower temperature and shorter annealing time, the α-Fe can't precipitate; Secondly, the precipitates are relatively small and cannot grow up in time, resulting in TEM equipment being unable to distinguish the α-Fe precipitate. And after annealing at 300 ℃ for 5 minutes, there are a large number of dislocations inside the alloy, and a small α-Fe precipitate is entangled with the dislocations, making it difficult to distinguish them.

The TEM image of the C19400 alloy annealed at 300 ℃ for 480 minutes is displayed in Figure 5. After annealing at 300 ℃ for 480 minutes, the dislocation density inside the alloy significantly decreased. Some large recovered grains gradually appear, and grain boundaries are also clearly observed, as displayed in Figures 5(a), (b), and (c). More importantly, after annealing at 300 ℃ for 480 minutes, a large number of dispersed a-Fe precipitates appeared inside the alloy. The a-Fe precipitates are mainly distributed at grain boundaries and dislocations. This is because in areas, such as grain boundaries and dislocations, the energy is higher and can provide a driving force for the precipitation process. Meanwhile, grain boundaries and dislocations can serve as channels for atomic diffusion, promoting further precipitation of the second phase. Similar results have been found in other reports [50, 51]. Through further analysis, it can be confirmed that after annealing at 300 °C for 480 minutes, the size of the a-Fe precipitate inside the C19400 alloy is about 31 nm, with a volume fraction of 1.15%, as seen in Figure S5(a). This dispersed distribution of fine a-Fe precipitates ensures the mechanical properties of the C19400 alloy, as presented in Figure 1. Even after annealing at 300 °C for 480 minutes, the decrease in the microhardness of the C19400 alloy is not significant. As is well known, the effect of annealing on alloys is contradictory. On the one hand, the annealing process will produce some small and dispersed second-phase particles, which will hinder dislocation slip through interactions with dislocations, thereby improving the mechanical properties of the alloy. On the other hand, annealing can cause the dislocation rearrangement and annihilation, resulting in a decrease in the dislocation density and softening of the alloy [52-54]. Next, high-resolution analysis was conducted at the interface between the a-Fe precipitates and Cu matrix, as shown in Figures 5(e) and (e_1). It can be clearly observed that the crystal plane spacing of a-Fe precipitates is 0.232 nm. According to Equation (8), the mismatch degree between the a-Fe and Cu matrix is 0.09. Therefore, there is a semi-coherent relationship between the α-Fe and Cu matrix. This conclusion is consistent with the results reported in other studies [19, 55]. Figure 5(f) indicates the diffraction patterns of the α-Fe precipitate and Cu matrix. The appearance of diffraction spots further proves the existence of the α-Fe precipitate.

In summary, after annealing at 300 °C for 5 and 480 minutes, there are dislocations and precipitates inside the C19400 alloy. As shown in Figures 1 and 2, after annealing at 300 °C for 5 minutes, the residual stress of the alloy was significantly reduced, but its hardness was improved. This feature is mainly because after annealing at 300 °C for 5 minutes, the strengthening effect of the precipitates is greater than the softening effect of annealing. After 90%-rolling deformation, the internal defects of the alloy increase sharply, which is conducive to the rapid precipitation of precipitates. And short-term annealing for 5 minutes is not enough to cause the precipitation phase to grow. Therefore, after annealing at 300 °C for 5 minutes, it mainly exists as dispersed and fine α-Fe precipitates, as analyzed earlier. This feature also explains why the α-Fe precipitate was not detected in Figure 4, but the alloy hardness still exhibits a precipitation-strengthening effect. Because in fact, after annealing at 300 °C for 5 minutes, the small α-Fe precipitates are covered by dense dislocations, making it difficult to detect. However, the precipitated phase of the α-Fe actually exists. Then, even annealing at 300 °C for 480 minutes can reduce the residual stress of the C19400 alloy, but after annealing for 480 minutes, the hardness of the alloy decreases, even if the decrease is not significant. This trend indicates that after annealing at 300 °C for

480 minutes, the softening effect of annealing is greater than the precipitation-hardening effect. Moreover, annealing for 480 minutes requires more time and cost compared to 5 minutes. Therefore, annealing at 300 °C for 5 minutes is a more suitable stress-relieving annealing process.

As exhibited in Figures 2 and S4, the C19400 alloy undergoes recrystallization after annealing at 500 °C. However, the residual-stress value after annealing at 500 °C is relatively high. Therefore, in order to explore this reason, further research was conducted on alloys annealed at 500 °C for 480 minutes.

Figure 6 reveals the TEM image of the C19400 alloy annealed at 500 °C for 480 minutes. It can be observed that even after annealing at 500 °C for 480 minutes, there are still dislocations inside the alloy. And a-Fe precipitates are distributed around the dislocations. From Figure 6(a), annealing twins can be observed with twin spacing of 600 and 667 nm. It is worth noting that annealing twins did not appear after annealing at 300 °C. By detecting the a-Fe precipitates, it can be observed that after annealing at 500 °C for 480 minutes, the a-Fe precipitates in the C19400 alloy grew to 82 nm, and the volume fraction decreased to 0.95%, as seen in Figure S5(b). This feature indicates that when the annealing temperature is increased from 300 °C to 500 °C, small a-Fe precipitates aggregate and rapidly grow, leading to a decrease in volume fraction. This process further led to a sharp decrease in the microhardness of the C19400 alloy after annealing at 500 °C for 480 minutes. According to the Orowan-strengthening mechanism [56-58], the finer and more dispersed the precipitates, the more favorable the increase in mechanical properties. Therefore, from Figures S4 and 6, it can be seen that the decrease in the microhardness of the C19400 alloy after annealing at 500 °C for 480 minutes is mainly due to the recrystallization behavior and the growth of precipitates. However, it is worth noting that even if recrystallization occurs at 500 °C, the residual stress of the alloy remains high. It is generally believed that as the temperature increases, the residual stress will decrease [59]. However, annealing at 500 °C revealed the opposite results. Some studies [60-62] suggest that the residual stress is related to the grain orientation and grain-size distribution. The presence of large-angle grain boundaries and twin boundaries can lead to thermal and plastic mismatches with surrounding grains, leading to the generation of the residual stress. In addition, there are relevant literatures [63, 64] reporting that the release of the residual stress is mainly through the recovery process, rather than through the recrystallization behavior. Indeed, the C19400 alloy exhibited significant recrystallization behavior after annealing at 500 °C, and obvious annealing twins can be observed from Figure 6(a). The above phenomena were not observed during annealing at 200 - 400 °C. That is to say, after high-temperature annealing at 500 °C, the grains inside the alloy transform from low-angle deformed grains to large-angle recrystallized grains, accompanied by the appearance of large-angle annealing twins. However, it is worth noting that after annealing at 500 °C, the alloy did not undergo complete recrystallization. This feature also means that after annealing at 500 °C, the interior of the alloy is mainly composed of recrystallized grains, accompanied by a small amount of un-recrystallized grains. As mentioned in the literature [60], there are thermal and plastic matching differences between these large-angle grains and the surrounding un-recrystallized grains. Therefore, both deformation and annealing processes can lead to the occurrence of the residual stress. More interestingly, through further observations, it was found that the residual stress after annealing at 500 ℃ for 5 minutes was smaller than that after annealing for 60 - 480 minutes. From Figure S4, it can be seen that after annealing at 500 ℃ for 5 minutes, the interior of the alloy is mainly composed of block-like recovered grains, and the recrystallized grains are almost invisible. This phenomenon is consistent with what is shown in Reference [63]. These results fully demonstrate that the release of the residual stress is mainly carried out through recovery rather than recrystallization. As is well known, the residual stress is an elastic distortion within an alloy. Therefore, the residual stress is mainly released through the thermal activation of dislocations. Although recrystallization at 500 ℃ can also reduce the dislocation density, incomplete recrystallization leads to an uneven grain-size distribution, which leads to the plastic mismatch and has a malignant effect. Moreover, from Figure 6, it can be seen that after annealing at 500 ℃ for 480 minutes, the α-Fe precipitates rapidly grow. As can be seen from the previous analysis, there is a semi-coherent relationship between the α-Fe precipitate and Cu matrix. Hence, there is already a certain degree of elastic distortion between the two. After the coarsening of the α-Fe, the elastic distortion between the α-Fe and Cu matrix may be greater, thereby increasing the residual stress of the C19400 alloy.

Dislocation evolution and residual-stress relaxation mechanism of the C19400 alloy after annealing

The evolution of the dislocation density is crucial for the residual stress. From the above discussion, it can be seen that the residual stress of the alloy after annealing at 300 °C is generally lower. Therefore, the dislocation density of the C19400 alloy annealed at 300 °C was quantitatively calculated, using the XRD technology. The calculation of the dislocation density can be simplified as follows [65]:

$$\rho = 16.1 \times \varepsilon^2 / b^2 \tag{9}$$

where ε is the alloy's lattice strain, b is the Burger vector of the copper alloy, approximately 0.256 nm. The lattice strain (ε) of the alloy can be obtained by fitting following equation [66, 67]:

$$FW \cdot cos\theta = 4\varepsilon \cdot sin\theta + K\lambda/D \tag{10}$$

where FW is the XRD peak broadening, and θ is the Bragg angle of the peak. K is a constant, approximately 1, λ =0.15 nm is the wavelength of the Cu-Kα radiation, and D represents the grain size.

Figure 7(a) indicates the XRD patterns of the C19400 alloy annealed at 300 °C for different times. It can be seen that after annealing at 300 °C for different times, the alloy mainly presents FCC and BCC phases. The FCC is the Cu matrix, while the BCC is the α-Fe precipitate. What's more, it can be inferred from the changes in the diffraction-peak intensity that there is a texture transformation inside the alloy after annealing at different times, which was discussed in detail in our previous work [31]. Figure 7(b) gives the dislocation density of the alloy annealed at 300 °C for different times, and the specific values are listed in Table 3. After annealing at 300 °C for 0 minutes, the dislocation density of the alloy was $8.68 \times 10^{14}\ \mathrm{m}^{-2}$. Then, with the increase of the annealing time, the dislocation density of the alloy indicated a gradually decreasing trend. After annealing at 300 °C for 480 minutes, the dislocation density of the alloy reached its lowest value of $5.53 \times 10^{14}\ \mathrm{m}^{-2}$. Compared to annealing for 0 minutes, the decrease rate of the dislocation density after annealing for 480 minutes was 36.3%. It is worth noting that during the entire annealing process, the dislocation density of the alloy did not change by an order of magnitude. To some extent, it proves that after annealing at 300 °C, the alloy mainly undergoes a recovery process. This result is consistent with the discussion above. That is to say, for the C19400 alloy, the recovery process is more conducive to the reduction of the residual stress in the alloy.

It is worth mentioning that although the alloy is mainly composed of a restored structure after annealing at 200 °C and 400 °C, their residual stress is still relatively high. This is mainly because when the alloy is annealed at 200 °C, the recovery effect inside the alloy is not as significant as at 300 °C due to the lower temperature. Then, when annealed at a low temperature of 200 °C, the heating rate of the alloy itself is slower. After holding at 200 °C for a certain period of time, the alloy core and surface cannot reach the same temperature at the same time. This temperature difference between inside and outside can easily lead to non-uniformity in the microstructure, which ultimately manifests as residual stresses.

However, the annealing of the C19400 alloy at 400 ℃ is completely opposite to that at 200 ℃. When annealed at 400 ℃, due to the higher temperature, the core and surface of the alloy will quickly reach the same temperature, especially for longer periods of time. Therefore, at the 400 ℃ insulation, a relatively uniform recovery process occurs inside the alloy. More importantly, during the cooling process of the alloy, due to its high temperature, the cooling rate of the alloy will also be faster, compared to 200 ℃ to ensure that it can quickly maintain consistency with room temperature. Therefore, during the cooling process, the cooling rate inside the alloy and the core is not consistent. Usually, the cooling rate of the alloy surface is greater than that of the core. Finally, due to the inconsistent cooling rate, a plastic mismatch occurred inside the alloy, leading to the increase of residual stress.

To sum up, compared to 200℃, 400 ℃, and 500 ℃, 300 ℃ is a turning point. Less than 300 ℃ will cause the residual stress in the alloy during heating due to inconsistent heating rates, while greater than 300 ℃ will cause an increase in the residual stress during cooling due to differences in cooling rates.

Figure 8 unveils the inverse fast Fourier transform (IFFT) diagrams of the alloy annealed at 300 ℃ for 5 minutes, 480 minutes and 500 ℃ for 480 minutes. It can be clearly observed that regardless of the annealing temperature, the dislocation is mainly concentrated between the precipitate phase and the matrix interface. Whether it is Fe_3P or α-Fe precipitates, dislocations will entangle at their interface with the Cu matrix. In this case, the interface will be in a state of high energy, and lattice distortion will be more pronounced, leading to the generation of the residual stress at the interface. Similar phenomena have appeared in other reports [68, 69]. On the advantageous side, the entanglement of precipitates, dislocations, and interfaces can seriously hinder the slip of dislocations, thereby greatly improving the mechanical properties of the C19400 alloy.

In order to summarize the evolution process of the microstructure, residual stress, and mechanical properties of the C19400 alloy during annealing, a schematic diagram is displayed in Figure 9. Firstly, when the C19400 alloy is annealed at 200 °C, due to the lower annealing temperature, the alloy still maintains the main characteristics of the rolled alloy. The dislocation density of the alloy is relatively high, and the grain boundaries are mainly distributed parallel to the rolling direction. Furthermore, both the small α-Fe and coarse Fe_3P were detected. Due to the interaction between dense precipitates, grain boundaries and dislocations, the residual stress is relatively high. And annealing did not reduce the residual stress due to the influence of heating rate. Then, as the temperature increases to 300 °C, the dislocation density of the alloy decreases and more α-Fe precipitates are generated. These small precipitates have a pinning effect on dislocations, leading to an improvement in the mechanical properties of the alloy. Moreover, after annealing at 300 °C, the recovery structure becomes more uniform, and the residual stress is effectively reduced. As the temperature continues to increase to 400 °C, the dislocation density of the alloy also decreases significantly, but the residual stress does not decrease. This trend is mainly attributed to the plastic mismatch caused by the cooling rate. Finally, after annealing at 500 ℃, the microstructure of the C19400 alloy underwent significant changes. The alloy is mainly composed of recrystallized grains. Moreover, the fine α-Fe coarsen due to aggregation, and the volume fraction also slightly decreases. However, due to the uneven distribution of grain sizes and differences of grain orientations, the decrease of the residual stress is not significant.

Conclusions

The microstructure, residual stress, and mechanical properties of the C19400 alloy annealed by different processes were studied. The most suitable stress-relieving annealing process has been proposed. The evolution of the residual stress of the C19400 alloy after annealing at different temperatures is discussed in detail. The effects of dislocations and precipitation on the residual stress and mechanical properties have been revealed. The main conclusions can be summarized as follows:

(1) After annealing at 200℃, 300℃, and 400 ℃, the microhardness of the C19400 alloy did not decrease significantly. However, after annealing at 500 ℃ for 60 minutes, the microhardness of the alloy exhibited a significant decrease. The microhardness decreased from 143.4 HV after 90%-rolling deformation to 97.6 HV after annealing. The decrease rate of microhardness is 31.9%. This is mainly because the alloy undergoes recrystallization after annealing at 500 ℃ for 60

minutes.

(2) For the C19400 alloy, annealing at 300 ℃ for 5 minutes is the optimal stress-relieving annealing process. Because after annealing at 300 ℃ for 5 minutes, the residual stress decreased from 125.9 MPa (RD) and 137.1 MPa (TD) to 13.2 MPa (RD) and 16.5 MPa (TD), with a decrease rate of 89.5% (RD) and 87.9% (TD), respectively.

(3) The release of the residual stress is mainly achieved through the recovery phenomenon occurring during the annealing process. Moreover, the high residual stress after recrystallization at 500 ℃ is mainly due to the presence of high-angle grain boundaries and annealing twins, which can lead to the plastic mismatch of surrounding grains.

(4) The a-Fe precipitate maintains the semi-coherent relationship with the Cu matrix. And after annealing at 300 ℃ for 480 minutes, the size of the a-Fe precipitate is about 31 nm, with a volume fraction of 1.15%. After annealing at 500 ℃ for 480 minutes, the a-Fe undergoes coarsening due to aggregation, with a size of approximately 82 nm and a volume fraction of 0.95%. The coarsening of precipitates can lead to the increase of the elastic strain, thereby increasing the residual stress of the C19400 alloy.

CRedit authorship contribution statement

T.F. Cao: Conceptualization, Investigation, Validation, Formal analysis, Data curation, Writing - original draft. **S.H. Wang:** Validation, Investigation. **P.K. Liaw:** Writing - review & editing, Visualization. **J.W. Qiao:** Conceptualization, Validation, Writing - review & editing, Supervision, Project administration, Funding acquisition.

Declaration of competing interest

The authors declare that they have no known competing financial interests or personal relationships that could have appeared to influence the work reported in this paper.

Data availability

Data will be made available on request.

Acknowledgement

The authors would like to acknowledge the financial support of the Key Research and Development Program of the Shanxi Province (No. 202102050201008). PKL very much appreciates the support from the National Science Foundation (DMR -1611180, 1809640, and 2226508).

References

[1] Z. Zheng, L. Zhang, W. Song, S. Feng, H. Xu, J. Sun, S. Yang, T. Chen, J. Wei, K.J. Chen, Gallium nitride-based complementary logic integrated circuits, Nature Electronics 4(8) (2021) 595-603.

[2] M.J.R. Heck, J.F. Bauters, M.L. Davenport, J.K. Doylend, S. Jain, G. Kurczveil, S. Srinivasan, Y. Tang, J.E. Bowers, Hybrid silicon photonic integrated circuit technology, IEEE Journal of Selected Topics in Quantum Electronics 19(4) (2013) 1-17.

[3] D.C. Ko, I.S. Lee, B.M. Kim, Consideration of buckling characteristics for optimal design of stiffened punch in the blanking process of lead frame, Journal of Materials Processing Technology 201(1) (2008) 273-279.

[4] X. Sun, J. Jie, T. Wang, T. Li, Effect of two-step cryorolling and aging on mechanical and electrical properties of a Cu-Cr-Ni-Si alloy for lead frames applications, Materials Science and Engineering: A 809 (2021) 1-11.

[5] S. Fu, P. Liu, X. Chen, H. Zhou, F. Ma, W. Li, K. Zhang, Effect of aging process on the microstructure and properties of Cu-Cr-Ti alloy, Materials Science and Engineering: A 802 (2021) 1-9.

[6] H. Fu, Y. Zhang, M. Zhang, X. Yun, Microstructure evolution, precipitation behavior, and mechanical properties of continuously extruded Cu-Ni-Si alloys at different aging treatments, Journal of Materials Processing Technology 317 (2023) 1-12.

[7] W. Liao, H. Yang, C. Yi, J. Zheng, Effect and mechanism of cold rolling and aging process on microstructure and properties of columnar grain C70250 copper alloy, Materials Science and Engineering: A 833 (2022) 1-12.

[8] X.B. Li, G.M. Jiang, J.P. Di, Y. Yang, C.L. Wang, Effect of cryogenic rolling on the microstructural evolution and mechanical properties of pure copper sheet, Materials Science and Engineering: A 772 (2020) 1-10.

[9] H.H. Lee, J.I. Yoon, H.K. Park, H.S. Kim, Unique microstructure and simultaneous enhancements of strength and ductility in gradient-microstructured Cu sheet produced by single-roll angular-rolling, Acta Materialia 166 (2019) 638-649.

[10] N. Forouzanmehr, M. Nili-Ahmadabadi, M. Samadi Khoshkhoo, On the microstructure and mechanical properties of severely cold shape rolled Cu, Materials Science and Engineering: A 650 (2016) 264-272.

[11] R. Li, Z. Xiao, Z. Li, X. Meng, X. Wang, Work hardening behavior and microstructure evolution of a Cu-Ti-Cr-Mg alloy during room temperature and cryogenic rolling, Materials 16(1) (2023) 1-15.

[12] S.S. Vadlamani, J. Eickemeyer, L. Schultz, B. Holzapfel, Rolling and recrystallisation textures in Cu-Al, Cu-Mn and Cu-Ni alloys, Journal of Materials Science 42(17) (2007) 7586-7591.

[13] N.R. Bochvar, O.V. Rybalchenko, D.V. Shangina, S.V. Dobatkin, Effect of equal-channel angular pressing on the precipitation kinetics in Cu-Cr-Hf alloys, Materials Science and Engineering: A 757 (2019) 84-87.

[14] M. Ma, X. Zhang, Z. Li, Z. Xiao, H. Jiang, Z. Xia, H. Huang, Effect of equal

channel angular pressing on microstructure and mechanical properties of a Cu-Mg Alloy, Crystals 10(6) (2020) 1-13.

[15] A. Korneva, B. Straumal, A. Kilmametov, L. Lityńska-Dobrzyńska, G. Cios, P. Bała, P. Zięba, Effect of high pressure torsion on microstructure of Cu-Sn alloys with different content of hume rothery phase, Materials Characterization 118 (2016) 411-416.

[16] O.V. Rybalchenko, N.R. Bochvar, G.V. Rybalchenko, N.S. Martynenko, N.Y. Tabachkova, S.V. Dobatkin, Comparative analysis of the aging kinetics in low-alloyed Cu-Cr-Hf and Cu-Cr-Zr alloys after high pressure torsion, Journal of Alloys and Compounds 955 (2023) 1-9.

[17] D. Yuan, X. Xiao, X. Luo, H. Wang, B. Han, B. Liu, B. Yang, Effect of multi-stage thermomechanical treatment on Fe phase evolution and properties of Cu-6.5Fe-0.3Mg alloy, Materials Characterization 185 (2022) 1-11.

[18] M. Wang, Y. Jiang, Z. Li, Z. Xiao, S. Gong, W. Qiu, Q. Lei, Microstructure evolution and deformation behaviour of Cu-10 wt%Fe alloy during cold rolling, Materials Science and Engineering: A 801 (2021) 1-10.

[19] F. Zhou, Y. Zhang, L. Lu, K. Song, H. Gao, Effects of a thermal-ultrasonic stress relaxation process on the residual stress, mechanical properties and microstructures of C19400 copper alloy strips, Materials Science and Engineering: A 841 (2022) 1-13.

[20] P. Vishnoi, S.M. Ishtiaque, A. Das, Effect of opening roller speed, drums speed difference and suction air pressure on properties of open-end friction spun polyester and acrylic yarns, Fibers and Polymers 6(3) (2005) 250-258.

[21] L. Qiu, S. Liu, X. Chen, Z. Wang, Lubrication and loading characteristics of cylindrical roller bearings with misalignment and roller modifications, Tribology International 165 (2022) 1-14.

[22] N. Sidhom, K. Makhlouf, A. Khlifi, C. Braham, H. Sidhom, Assessment of low cycle fatigue improvement of machined AISI 316 stainless steel by brush hammering, Fatigue & Fracture of Engineering Materials & Structures 37(10) (2014) 1087-1100.

[23] N. Sidhom, N.B. Moussa, S. Janeb, C. Braham, H. Sidhom, Potential fatigue strength improvement of AA 5083-H111 notched parts by wire brush hammering: Experimental analysis and numerical simulation, Materials & Design 64 (2014) 503-519.

[24] X.X. Tu, L.R. Xiao, Z.Y. Cai, Z.W. Peng, P.H. Ren, D.L. Zeng, X.J. Zhao, Effects of vibration aging on residual stress and performance of instrument-grade TiC reinforced steel matrix composite, Materials Letters 325 (2022) 1-5.

[25] J.-S. Wang, C.-C. Hsieh, H.-H. Lai, C.-W. Kuo, P.T.-Y. Wu, W. Wu, The relationships between residual stress relaxation and texture development in AZ31 Mg alloys via the vibratory stress relief technique, Materials Characterization 99 (2015) 248-253.

[26] A. Ellermann, B. Scholtes, Residual stress states as a result of bending and straightening processes of steels in different heat treatment conditions, International Journal of Materials Research 103(1) (2012) 57-65.

[27] Y. Zhang, S. Li, K. Song, Y. Zhou, F. Zhou, L. Lu, A. Liu, Effect of stretch-bending straightening on the residual stress of C19400 alloy strips, Journal of Materials Engineering and Performance 32(4) (2023) 1883-1891.

[28] Y. Zhan, H. Xu, W. Du, C. Liu, Research on the influence of heat treatment on residual stress of TC4 alloy produced by laser additive manufacturing based on laser ultrasonic technique, Ultrasonics 115 (2021) 1-10.

[29] M. Honarpisheh, F. Nazari, M.A. Haghighi, Annealing heat treatment effect on the residual stresses in hot-extruded aluminum alloy rods with high cross-sectional reduction, Strength of Materials 52(2) (2020) 291-302.

[30] Z.-H. Gao, H.-J. Gao, Y.-D. Zhang, Q. Wu, Experiment and mechanism investigation on the effect of heat treatment on residual stress and mechanical properties of SiCp/Al-Cu-Mg composites, Materials Science and Engineering: A 884 (2023) 1-16.

[31] T. Cao, S. Wang, G. Zhao, X. Wu, P.K. Liaw, J. Qiao, Evolution of microstructure and residual stress for a lead-frame Cu-2.13Fe-0.026 P (wt%) alloy, Journal of Alloys and Compounds 965 (2023) 1-16.

[32] Q. Lei, Z. Li, C. Dai, J. Wang, X. Chen, J.M. Xie, W.W. Yang, D.L. Chen, Effect of aluminum on microstructure and property of Cu-Ni-Si alloys, Materials Science and Engineering: A 572 (2013) 65-74.

[33] Y. Ye, X. Yang, J. Wang, X. Zhang, Z. Zhang, T. Sakai, Enhanced strength and electrical conductivity of Cu-Zr-B alloy by double deformation-aging process, Journal of Alloys and Compounds 615 (2014) 249-254.

[34] T. Guo, J. Li, J. Wang, W.Y. Wang, Y. Liu, X. Luo, H. Kou, E. Beaugnon, Microstructure and properties of bulk Al0.5CoCrFeNi high-entropy alloy by cold rolling and subsequent annealing, Materials Science and Engineering: A 729 (2018) 141-148.

[35] T. Cao, P. Su, Z. Xu, Z. Feng, S. Wang, J. Qiao, Evaluation of residual stress in lead frame copper strips by nanoindentation, Journal of Materials Science 58 (2023) 5884-5900.

[36] F. Nazari, M. Honarpisheh, H. Zhao, Effect of stress relief annealing on microstructure, mechanical properties, and residual stress of a copper sheet in the constrained groove pressing process, The International Journal of Advanced Manufacturing Technology 102(9-12) (2019) 4361-4370.

[37] J. Liu, Z. Du, J. Su, J. Tang, F. Jiang, D. Fu, J. Teng, H. Zhang, Effect of quenching residual stress on precipitation behaviour of 7085 aluminium alloy, Journal of Materials Science & Technology 132 (2023) 154-165.

[38] W. Chen, Z.S. You, N.R. Tao, Z.H. Jin, L. Lu, Mechanically-induced grain coarsening in gradient nano-grained copper, Acta Materialia 125 (2017) 255-264.

[39] V. Subramanya Sarma, K. Sivaprasad, D. Sturm, M. Heilmaier, Microstructure and mechanical properties of ultra fine grained Cu-Zn and Cu-Al alloys produced by cryorolling and annealing, Materials Science and Engineering: A 489(1-2) (2008) 253-258.

[40] J. Gao, S. Jiang, H. Zhang, Y. Huang, D. Guan, Y. Xu, S. Guan, L.A. Bendersky,

A.V. Davydov, Y. Wu, H. Zhu, Y. Wang, Z. Lu, W.M. Rainforth, Facile route to bulk ultrafine-grain steels for high strength and ductility, Nature 590(7845) (2021) 262-267.

[41] R. Nivas, G. Das, S.K. Das, B. Mahato, S. Kumar, K. Sivaprasad, P.K. Singh, M. Ghosh, Effect of stress relief annealing on microstructure & mechanical properties of welded joints between low alloy carbon steel and stainless steel, Metallurgical and Materials Transactions A 48(1) (2017) 230-245.

[42] Q. Chao, S. Thomas, N. Birbilis, P. Cizek, P.D. Hodgson, D. Fabijanic, The effect of post-processing heat treatment on the microstructure, residual stress and mechanical properties of selective laser melted 316L stainless steel, Materials Science and Engineering: A 821 (2021) 1-13.

[43] A. Muiruri, M. Maringa, W. du Preez, L. Masu, Effect of stress-relieving heat treatment on the high strain rate dynamic compressive properties of additively manufactured Ti6Al4V (ELI), Metals 10(5) (2020) 1-19.

[44] H. Cao, J.Y. Min, S.D. Wu, A.P. Xian, J.K. Shang, Pinning of grain boundaries by second phase particles in equal-channel angularly pressed Cu-Fe-P alloy, Materials Science and Engineering: A 431(1-2) (2006) 86-91.

[45] H. Miura, H. Tsukawaki, T. Sakai, J.J. Jonas, Effect of particle/matrix interfacial character on the high-temperature deformation and recrystallization behavior of Cu with dispersed Fe particles, Acta Materialia 56(17) (2008) 4944-4952.

[46] D.G. Morris, M.A. Muñoz-Morris, The effectiveness of equal channel angular pressing and rod rolling for refining microstructures and obtaining high strength in a Cu-Fe composite, Materials Science and Engineering: A 528(19-20) (2011) 6293-6302.

[47] L. Dirand, J. Cormier, A. Jacques, J.-P. Chateau-Cornu, T. Schenk, O. Ferry, P. Bastie, Measurement of the effective γ/γ′ lattice mismatch during high temperature creep of Ni-based single crystal superalloy, Materials Characterization 77 (2013) 32-46.

[48] M. Hoelzel, D. Del Genovese, R. Gilles, D. Mukherji, D.M. Toebbens, J. Roesler, H. Fuess, Phase analysis and lattice mismatches in superalloys DT706 and Inconel 706, Physica B: Condensed Matter 385-386 (2006) 594-596.

[49] F. Pyczak, A. Bauer, M. Göken, U. Lorenz, S. Neumeier, M. Oehring, J. Paul, N. Schell, A. Schreyer, A. Stark, F. Symanzik, The effect of tungsten content on the properties of L12-hardened Co-Al-W alloys, Journal of Alloys and Compounds 632 (2015) 110-115.

[50] Q. Dong, M. Wang, L. Shen, Y. Jia, Z. Li, Diffraction analysis of α-Fe precipitates in a polycrystalline Cu-Fe alloy, Materials Characterization 105 (2015) 129-135.

[51] Y. Fujimura, T. Matsui, S. Semboshi, Y. Okamoto, K. Nishida, Y. Yamamoto, A. Iwase, Structure of thermal-aging induced Fe clusters and their effects on physical properties for Cu-1.2 at.% Fe alloy, Journal of Alloys and Compounds 682 (2016) 805-814.

[52] S.J. Park, S.-H. Jo, J.G. Kim, J. Kim, R. Lee, Y.-S. Oh, S.-J. Kim, H.W. Lee, S.-H. Kang, J. Jung, Evolution of microstructure, mechanical properties and residual stress of a cold rolled Invar sheet due to heat treatment, Metals 12(1) (2022) 1-9.

[53] T. Yamashita, N. Koga, T. Kawasaki, S. Morooka, S. Tomono, O. Umezawa, S. Harjo, Work hardening behavior of dual phase copper-iron alloy at low temperature, Materials Science and Engineering: A 819 (2021) 1-10.

[54] M.X. Guo, J. Zhu, L. Yi, F. Wang, G.J. Li, R.S. Lei, Effects of precipitation and strain-induced martensitic transformation of Fe-C phases on the mechanical properties of Cu-Fe-C alloy, Materials Science and Engineering: A 697 (2017) 119-125.

[55] H.G. Kim, T.W. Lee, S.Z. Han, K. Euh, W.-Y. Kim, S.H. Lim, Microstructural study on effects of C-alloying on Cu-Fe-P cast alloy, Metals and Materials International 18(2) (2012) 335-339.

[56] Z. Zhang, D.L. Chen, Contribution of orowan strengthening effect in particulate-reinforced metal matrix nanocomposites, Materials Science and Engineering: A 483-484 (2008) 148-152.

[57] J.F. Nie, B.C. Muddle, Strengthening of an Al-Cu-Sn alloy by deformation-resistant precipitate plates, Acta Materialia 56(14) (2008) 3490-3501.

[58] S. Xu, Z. Zhou, F. Long, H. Jia, N. Guo, Z. Yao, M.R. Daymond, Combination of back stress strengthening and orowan strengthening in bimodal structured Fe-9Cr-Al ODS steel with high Al addition, Materials Science and Engineering: A 739 (2019) 45-52.

[59] Y. Sun, F. Jiang, H. Zhang, J. Su, W. Yuan, Residual stress relief in Al-Zn-Mg-Cu alloy by a new multistage interrupted artificial aging treatment, Materials & Design 92 (2016) 281-287.

[60] Y. Wan, W. Jiang, M. Song, Y. Huang, J. Li, G. Sun, Y. Shi, X. Zhai, X. Zhao, L. Ren, Distribution and formation mechanism of residual stress in duplex stainless steel weld joint by neutron diffraction and electron backscatter diffraction, Materials & Design 181 (2019) 1-10.

[61] R.L.P. Y.D. Wang, X.-L. Wang, R.L. McGreevy, Grain-orientation-dependent residual stress and the effect of annealing in cold-rolled stainless steel, Acta Materialia 50 (2002) 1717-1734.

[62] K.K.C. Y.H. Chung, J.H. Han and M.C. Shin, Effect of grain shape and texture on the earings in an Al-Li alloy, Scripta Materialia 43 (2000) 759-764.

[63] R. Wawszczak, A. Baczmanski, C. Braham, W. Seiler, M. Wróbel, K. Wierzbanowski, Residual stresses in Austenitic steel during plastic deformation and recovery processes, Materials Science Forum 681 (2011) 223-228.

[64] I. Nikitin, M. Besel, Residual stress relaxation of deep-rolled austenitic steel, Scripta Materialia 58(3) (2008) 239-242.

[65] J. Li, H. Ding, B. Li, Study on the variation of properties of Cu-Cr-Zr alloy by different rolling and aging sequence, Materials Science and Engineering: A 802 (2021) 1-7.

[66] X.K. Zhang, X.Y. Yang, W. Chen, J. Qin, J.P. Fouse, Effect of stacking fault energy on mechanical properties and annealing behavior of brasses, Journal of Alloys and Compounds 679 (2016) 400-407.

[67] J. Hou, M. Zhang, S. Ma, P.K. Liaw, Y. Zhang, J. Qiao, Strengthening in

Al0.25CoCrFeNi high-entropy alloys by cold rolling, Materials Science and Engineering: A 707 (2017) 593-601.
[68] J. Yang, K. Bu, Y. Zhou, K. Song, T. Huang, X. Peng, H. Liu, Y. Du, Microstructure, residual stress, and mechanical properties evolution of a Cu-Fe-P alloy under different conditions, Journal of Materials Research and Technology 24 (2023) 7896-7909.
[69] H. Song, H. Gao, Q. Wu, Y. Zhang, Residual stress relief mechanisms of 2219 Al-Cu alloy by thermal stress relief method, Reviews on Advanced Materials Science 61(1) (2022) 102-116.

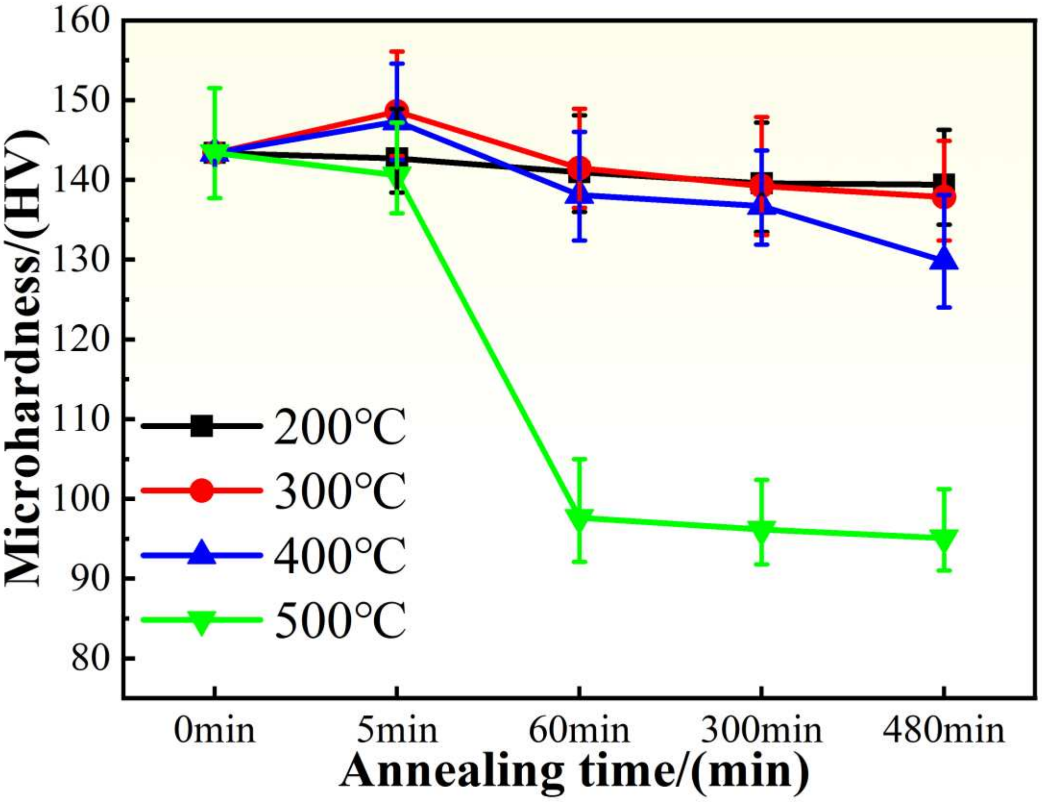

Figure 1. Microhardness of the C19400 alloy with 90%-cold-rolled deformation after annealing at different temperatures and times.

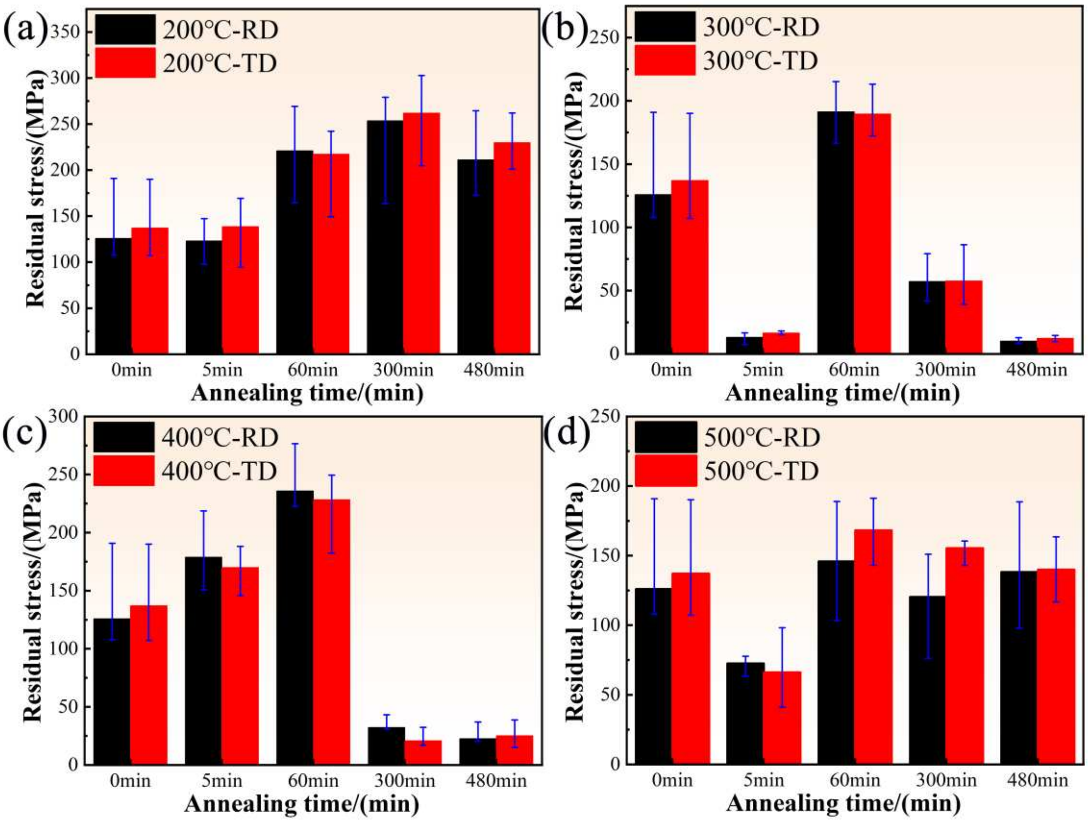

Figure 2. Residual stress in the rolling direction (RD) and transverse direction (TD) of the C19400 alloy with 90%-cold-rolling deformation after different annealing temperatures: (a) 200 °C; (b) 300 °C; (c) 400 °C; and (d) 500 °C.

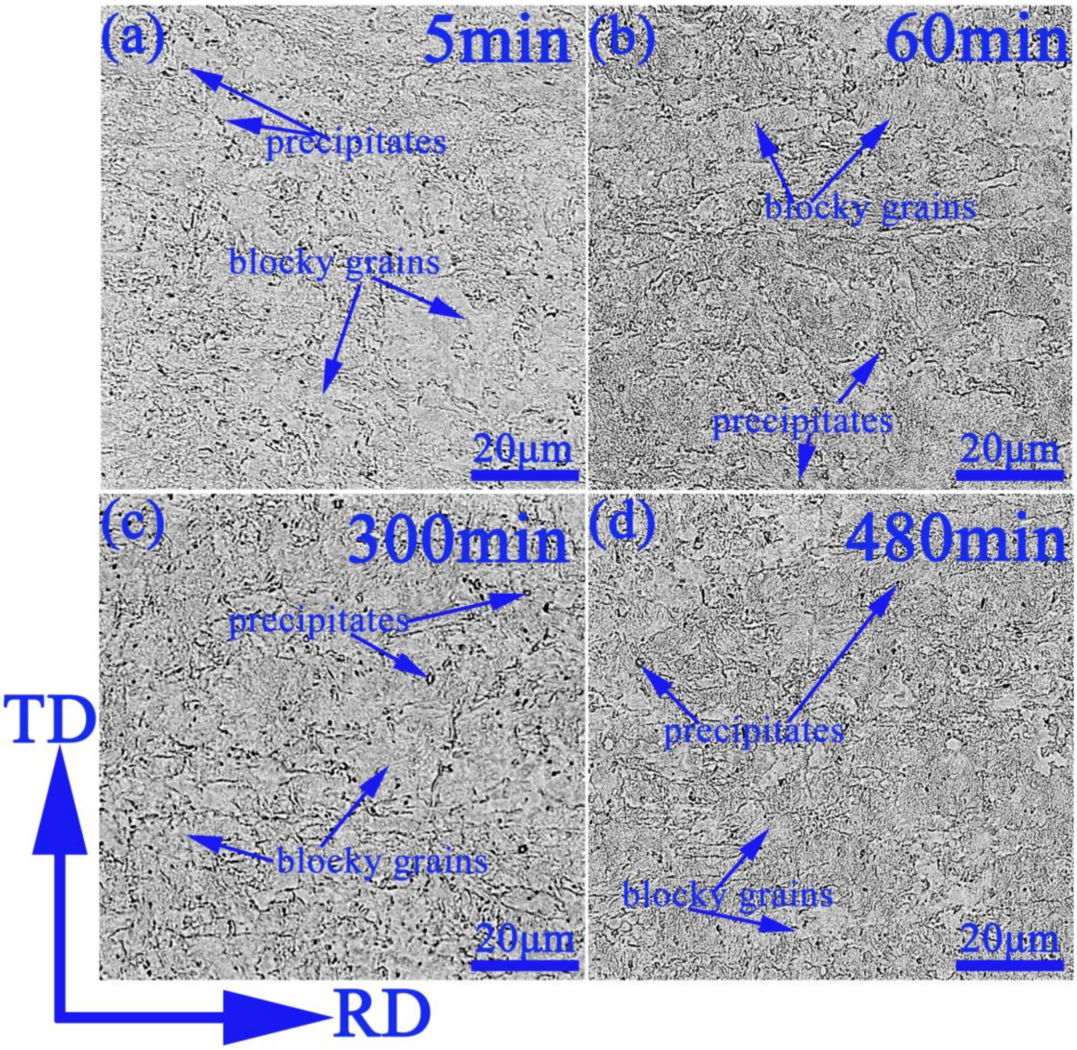

Figure 3. SEM images of the C19400 alloy with 90% cold-rolling deformation annealed at 300 °C for different times: (a) 5 min; (b) 60 min; (c) 300 min; and (d) 480 min.

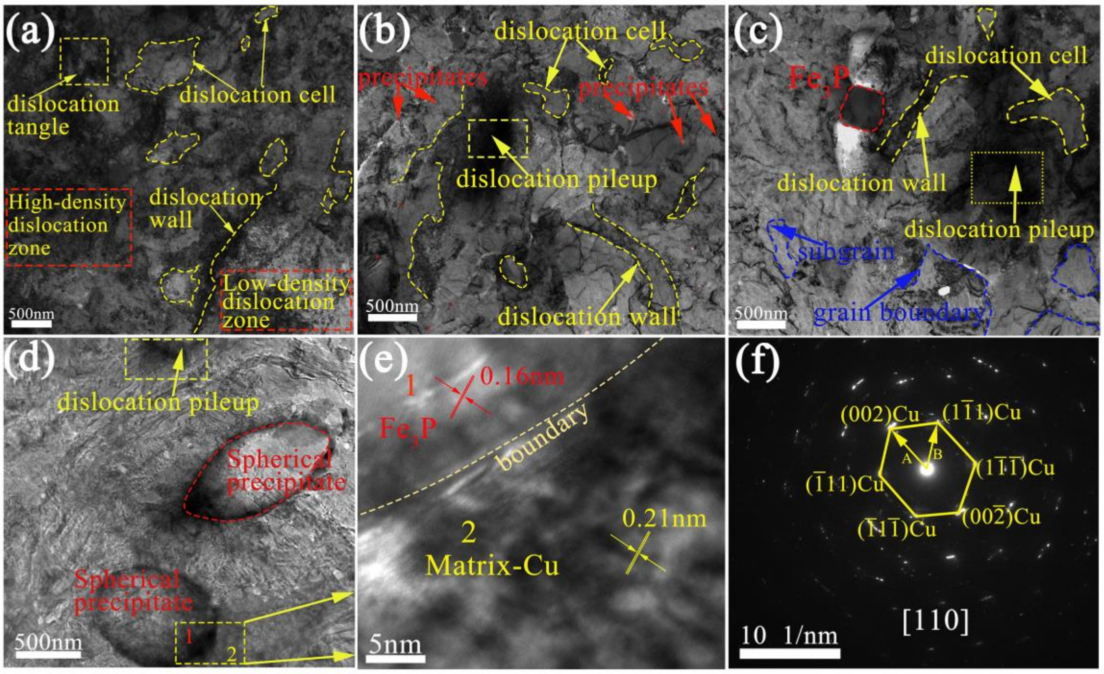

Figure 4. TEM micrographs of the C19400 alloy with 90%-cold rolling annealed at 300 ℃ for 5 minutes. (a)-(d) bright fields (BF) of dislocations and precipitates; (e) HRTEM image of yellow rectangular box in (d); and (f) selected area electron diffraction (SAED) of position 2 in (d).

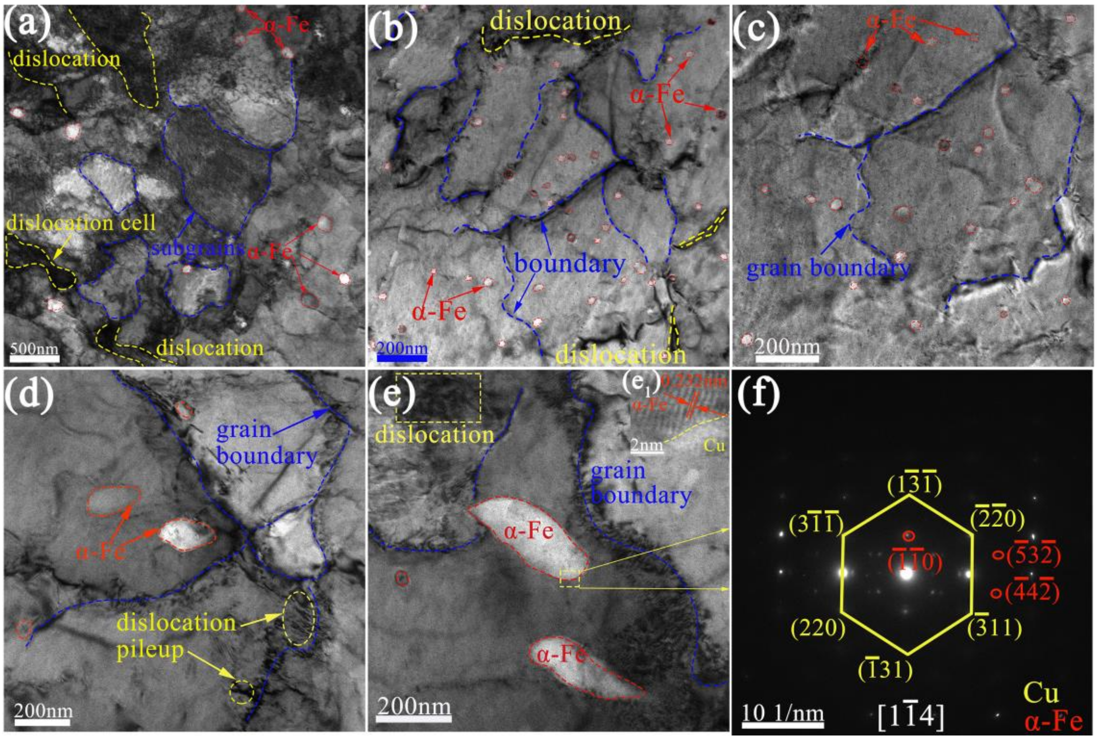

Figure 5. TEM micrographs of the C19400 alloy with 90- cold rolling annealed at 300 °C for 480 minutes. (a)-(e) BF of dislocations and precipitates; (e_1) HRTEM image of a yellow rectangular box in (e); and (f) SAED of a yellow rectangular box in (e).

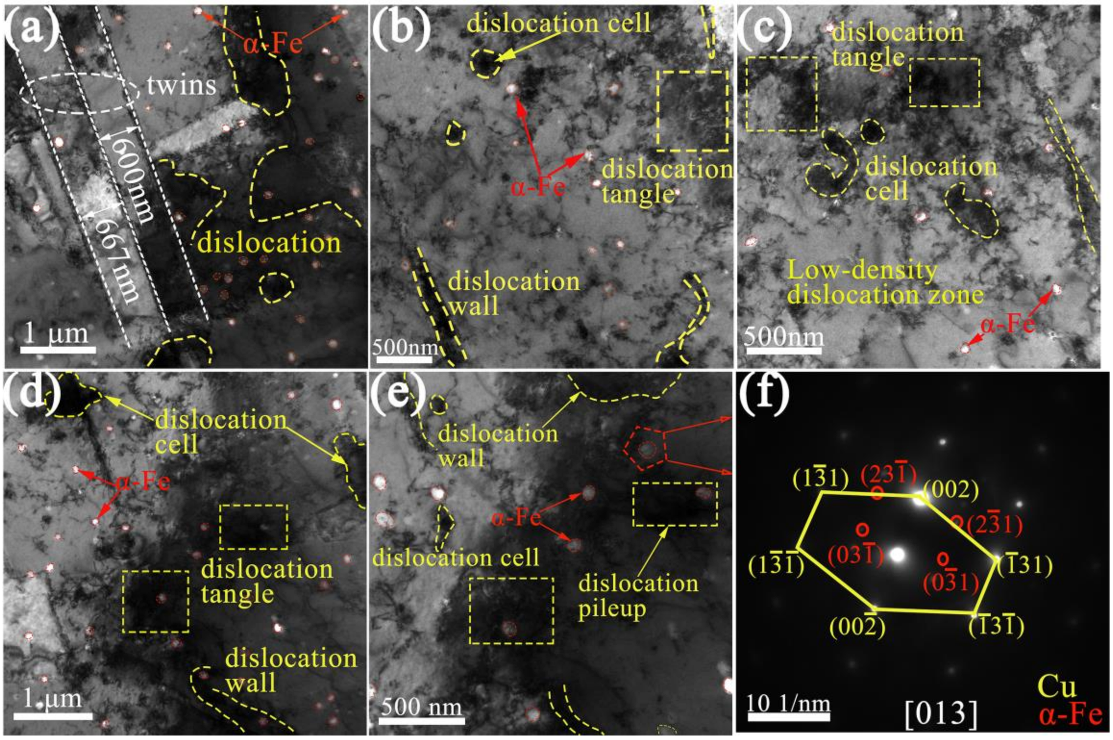

Figure 6. TEM micrographs of the C19400 alloy with 90%-cold rolling annealed at 500 ℃ for 480 minutes. (a)-(e) BF of dislocations, twins, and precipitates; and (f) SAED of a red box in (e).

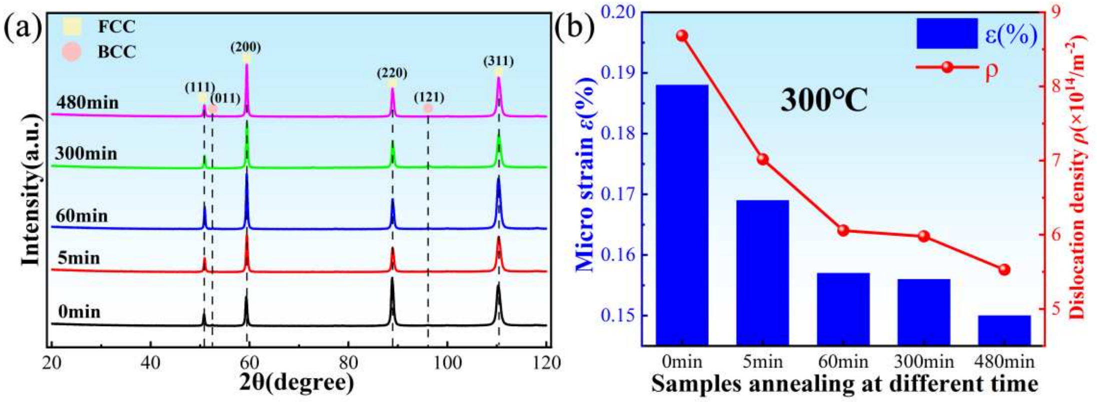

Figure 7. XRD pattern and dislocation density of the C19400 alloy after annealing at 300 °C for different times. (a) XRD pattern; and (b) lattice strain, ε and dislocation density, ρ.

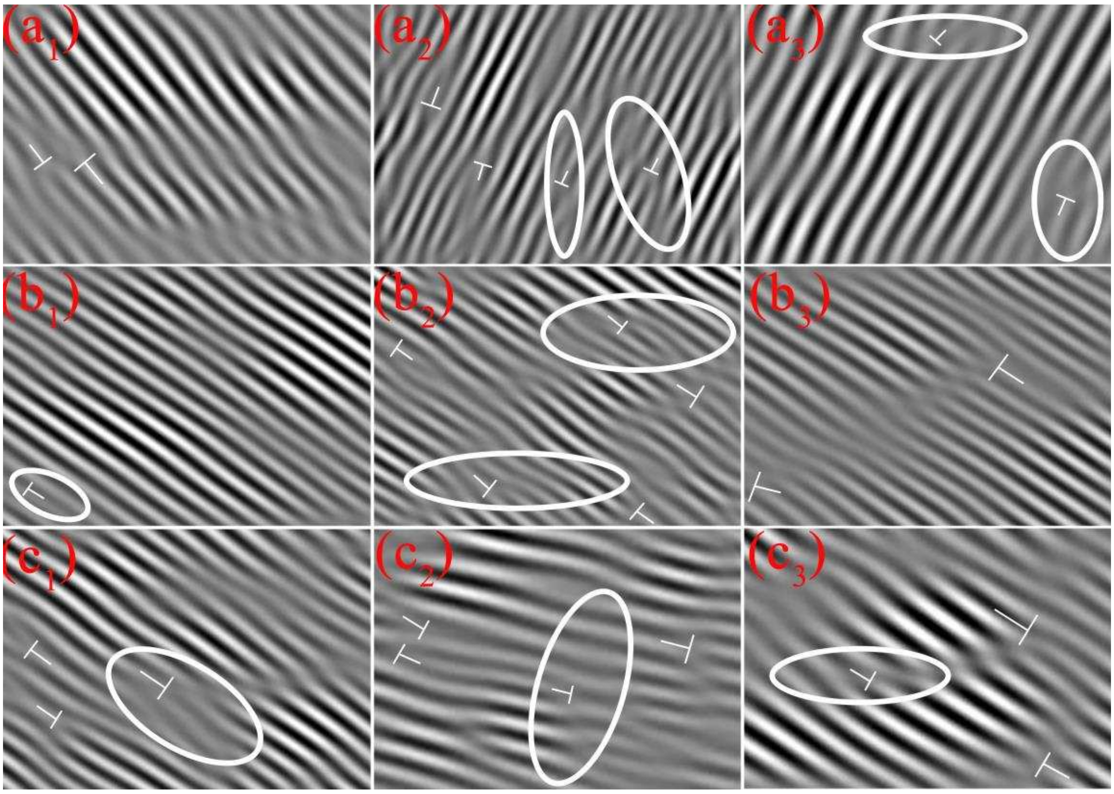

Figure 8. IFFT diagram that can reflect the distribution of dislocations. (a_1)-(a_3) the dislocation distribution of the precipitate, the interface between the precipitate and the matrix, and the Cu matrix after annealing at 300 ℃ for 5 minutes; (b_1)-(b_3) the dislocation distribution of the precipitate, the interface between the precipitate and the matrix, and the Cu matrix after annealing at 300 ℃ for 480 minutes; (c_1)-(c_3) the dislocation distribution of the precipitate, the interface between the precipitate and the matrix, and the Cu matrix after annealing at 500 ℃ for 480 minutes;

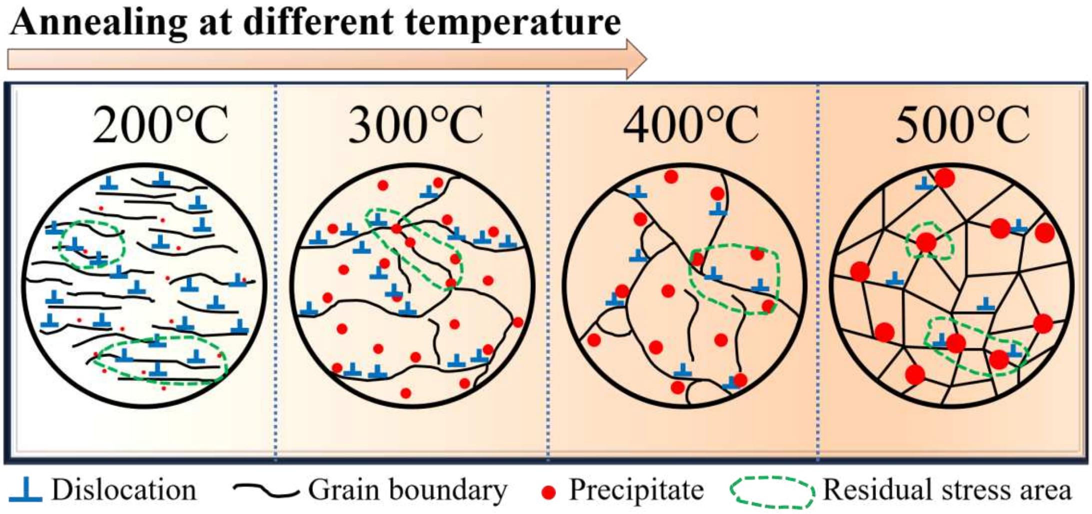

Figure 9. Schematic diagram of microstructure and residual-stress evolution of the C19400 alloy after annealing.

Table 1

Microhardness of the C19400 alloy after different annealing processes.

Microhardness	0 min	5 min	60 min	300 min	480 min
200 ℃	143.4	142.7	141.0	139.6	139.4
300 ℃	143.4	148.6	141.5	139.2	137.8
400 ℃	143.4	147.3	138.1	136.7	129.9
500 ℃	143.4	140.6	97.6	96.1	95.1

Table 2

Residual stress (MPa) of C19400 alloy after different annealing processes.

RD	0 min	5 min	60 min	300 min	480 min
200 °C	125.9	123.1	220.9	253.5	211.2
300 °C	125.9	13.2	191.3	57.3	9.9
400 °C	125.9	178.8	235.8	32.3	22.6
500 °C	125.9	72.5	145.8	120.3	138.2
TD	0 min	5 min	60 min	300 min	480 min
200 °C	137.1	138.5	217.2	261.9	229.9
300 °C	137.1	16.5	189.6	57.7	12.3
400 °C	137.1	169.9	228.3	20.8	25.1
500 °C	137.1	66.1	168.2	155.3	139.9

Table 3

Lattice strains, ε, and dislocation densities, ρ, of C19400 alloy after annealing at 300 °C for different time.

Time	0 min	5 min	60 min	300 min	480 min
ε (%)	0.188	0.169	0.157	0.156	0.150
ρ ($\times 10^{14}$ m^2)	8.683	7.016	6.055	5.979	5.527